International Journal of Impact Engineering 189 (2024) 104973

Contents lists available at ScienceDirect

International Journal of Impact Engineering

journal homepage: www.elsevier.com/locate/ijimpeng

Fast optimisation of honeycombs for impact protection

Olly Duncan

Manchester Metropolitan University, All Saints Campus, Manchester, M15 6BH, UK

ARTICLE INFO

Dataset link: https://data.mendeley.com/datasets/5fwrmywjjs/1 , https://meta-genome.org

Keywords:
Mechanical metamaterials
Micromechanics
Experimental mechanics
Finite element modelling

ABSTRACT

Cellular solids such as honeycombs are often used in impact protection systems. Those with precisely defined geometries allow responses to be programmed to specific functions, but can be costly to design. This article presents an analytical model for fast, parametric optimisation. The analytical model, and a numerical one, were validated against experimental data for three honeycomb variants, during compression tests to 80% engineering strain, and 1, 3 and 5 J impacts. The numerical model force readings remained within 5% of the experiments. A further verification of the analytical model, varying all parameters within the honeycomb geometry, was undertaken for 5 J and 15 J impacts. The analytical model predicted energy absorption at all displacement increments to be (on average) 3% higher than the numerical one. The limits of agreement (with 95% confidence) were between +15 and −9% of the numerical model. The analytical model provided solutions almost instantly, so was used in a demonstrative parametric optimisation study, for a 10 J impact. The input and output solutions were verified in the numerical model, showing a four-fold reduction in peak force (from ∼2000 to ∼500 N).

1. Introduction

Cellular solids are, and have long been, the primary choice for cushioning layers used in impact protection, spanning sports, healthcare, defence, transport and packaging [1–12]. While protective equipment traditionally uses foams, transformative developments in manufacturing and fabrication allow the geometry and patterning of cells in lattices and honeycombs to be precisely defined [1,2,13,14]. These rationally design structures with properties that cannot be achieved in the intrinsic materials they are made from are known as mechanical metamaterials [15]. Lattice and honeycomb cells can be arranged periodically (in a repeating pattern), aperiodically (varying randomly, discretely, or with a gradient), or have varying degrees of hierarchy (degrees of scales with recognised structure) [16–20,13].

Protective equipment serves various functions, with the core goal being to mitigate loading conditions associated with a high risk of injury (or damage). [21,2,1]. During impacts, injury risk is generally thought to increase with the magnitude of peak force or acceleration [2,22,23], the rate of application of such force [2,22,24], and the duration over which it is sustained [22,23]. Other factors which affect injury risk include impact direction and location, environmental conditions (e.g., temperature and humidity), elastic wave propagation, and whether the impact is blunt, or concentrated [22,24–28]. Similar factors also affect the likelihood of damage to materials or objects [4].

Honeycombs designed and tested with the intention of mitigating injury risk can be used out-of-plane (with straight walls approximately parallel to the impact direction) [29], or in-plane (with straight walls approximately perpendicular to the impact direction) [2,1,29–31]. When developing systems to protect objects, or for use under high energy and high speed impacts, the orientation is typically out of plane, using stiff materials that crush under impact [29]. Such crushing can be caused by a single fold, or a series of progressive folds, each causing a reduction and plateau in compression force [29]. Personal protective equipment for low energy impacts (e.g., sports, medical devices, or footwear), often uses in-plane honeycombs, or lattices [2,1,29,30,32]. These can be made from hyper-elastic, or highly viscoelastic material, meaning the protective device can withstand numerous impacts. Such honeycombs, or similar hyper-elastic lattices, offer comfort and flexibility, and additional opportunity to tune response to glancing or oblique impacts [33–36].

While mechanical metamaterials could improve products, including safety equipment, increased freedom to design multiscale structures brings new challenges. Concurrent, multi-scale optimisation of internal microsctructure and external macrostructure is computationally expensive [37,13,38]. Designing for large strains seen under impact, and integrating into multi-body simulations (e.g., including realistic human body surrogates, protective devices, and colliding objects) often makes computational design and optimisation unfeasible [2,38].

To leverage these new materials, industry uses mixed-method product developments cycles [2]. These often start with know-how, to generate a prototype that is improved experimentally, or by using microstructurally faithful finite element models [2,38,13]. Fast map-

E-mail address: o.duncan@mmu.ac.uk.

https://doi.org/10.1016/j.ijimpeng.2024.104973
Received 4 January 2024; Received in revised form 15 March 2024; Accepted 6 April 2024
Available online 9 April 2024

ping between micro-structure and property is well developed under low-strains, either using analytical methods [3,4,39–41], or by applying homogenisation to single cell geometries via. periodic boundary conditions (PBCs) [38,13]. Advanced, higher order methods also facilitate application of PBCs under large strains, by using additional terms to map micro and macro-deformations [42–44,37,45]. These still require robust development of characterisation protocols before they see widespread uptake [38]. Numerical methods remain the typical choice for computational honeycomb (and lattice) optimisation [35,34,36,33]. Once developed, the level of agreement between experiment and simulation is typically 5 to 10% [35,34,36,33].

Various machine learning, or artificial intelligence methods, are emerging for mechanical metamaterial design and optimisation [46,20,38,47]. After training, such methods rapidly generate structures for a wide variety of potential responses, with errors typically within 15% [46,20,38,47]. A broad variety of AI methods that includes large language models, neural networks, transformers, and video denoising, have been used [46,20,38,47]. These allow recognition and selection for known phenomena during deformation, such as cell wall or rib buckling during compression [46].

As an alternative, analytical methods have potential to facilitate fast approximation of large-strain response, via. the occurrence of buckling and self-contact, and the additional tensors required to map micro and macro deformations [17]. Current analytical models of cellular structures provide some benefits over generalised ones. In comparison to higher order continua (e.g., micromorphic ones [43]), analytical models provide direct mapping between geometry and response. Analytical models also offer stark reductions in computational cost, when compared to microstructurally faithful finite element models, as they do not require meshing [37]. Conversely, though, these models are generally constrained to a specific class of structure, are not generalised between structures, and do not usually extend to the large strains seen under impact [3,4,39,40,48–50].

Given that hexagonal honeycombs are found throughout structural engineering, mechanical metamaterials, and in biological systems (to name a few), large strain analytical models for these receive notable interest (e.g. [3,4,39,40,48–50]). Such analytical models have low set up and computational costs, and have been used to estimate the compressive response up until, and slightly beyond, the point where cells and cell walls buckle [4,40,39,17,51,48–50]. Under impact the stress vs. strain plateau phase between cell wall buckling and self-contact between cell walls (Fig. 1) is critical to performance; allowing energy absorption with minimal force increase (often proportional to injury risk - [1–11]).

This paper presents and validates a new analytical modelling approach for six-sided, centre-symmetric honeycombs under low-speed impacts, then uses the model to undertake a parametric optimisation. The structure is: introduction of the analytical modelling method, then experimental and microstructurally faithful FE validation and verification, leading to a parametric optimisation, followed by combined results and discussions. Editable Matlab implementations of the modelling and optimisation tools are made available [52].

2. Methods

2.1. Analytical modelling methods

As with traditional analytical models for honeycombs, [4,40,17], effective properties were obtained from cell geometries. As the load cases were all uniform compression and flat-plate impact, direct mapping between local and global stiffness matrices, stress and strain, and force and displacement, were assumed. During compression, most hexagonal honeycombs (or lattices and related systems) have three (well documented) deformation regions [4] (Fig. 1). At low levels of compression, the stress vs. strain response is linear. At approximately

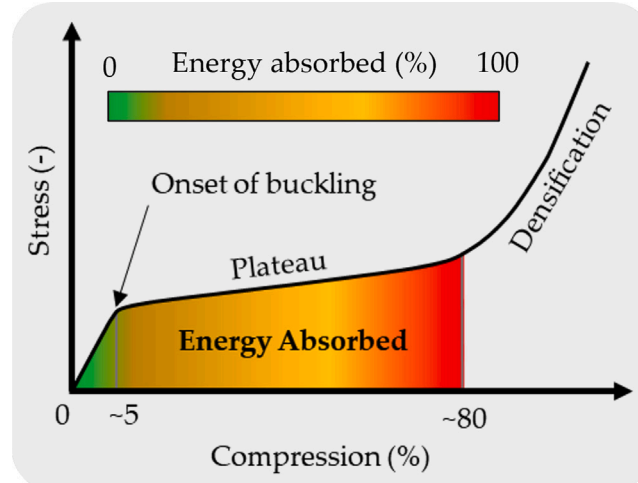

Fig. 1. Example honeycomb compressive response.

5% compression, cell walls may buckle — causing a relative plateau region whereby stress remains nearly constant, while compressive strain increases. Then, as density increases, cells walls undergo self-contact, causing a stark stiffness increase, tending towards that of the base material [4].

2.1.1. Pre-buckling

The geometry of a centre-symmetric, six sided honeycomb can be described by the angle of the oblique wall relative to the x-axis (θ), wall thickness (t), oblique wall length (l), vertical wall length (h), and cell orientation (ϕ) (Fig. 2a to e). Normalisation was undertaken to simplify the presentation of the equations for the local stiffness matrix of the unit-cell relative volume element; all dimensions were divided by the length of the oblique wall (l). The depth of the relative volume element (w) was also set to be equal to the oblique wall length (i.e., unity). During the relatively linear region of honeycomb stress vs. strain response, deformation occurs via. wall compression/tension, hinging at the junctions, and wall flexing (Fig. 2f to i).

The low-strain, elastic response of hexagonal honeycombs can be calculated based on unit-cell geometries, and base material properties [4,40,39]:

$$\nu_{xy} = \frac{\sin\theta\,\cos^2\theta\left(\frac{1}{K_{hf}} - \frac{1}{K_s}\right)}{\left(\frac{h}{l} + \sin\theta\right)\left[\frac{\sin^2\theta}{K_{hf}} + \frac{\cos^2\theta}{K_s}\right]} \tag{1}$$

$$\nu_{yx} = \frac{\sin\theta\left(\frac{h}{l} + \sin\theta\right)\left(\frac{1}{K_{hf}} - \frac{1}{K_s}\right)}{\left[\frac{\cos^2\theta}{K_{hf}} + \frac{\frac{2h}{l} + \sin^2\theta}{K_s}\right]} \tag{2}$$

$$E_x = \frac{\cos\theta}{t\left(\frac{h}{l} + \sin\theta\right)\left[\frac{\sin^2\theta}{K_{hf}} + \frac{\cos^2\theta}{K_s}\right]} \tag{3}$$

$$E_y = \frac{\frac{h}{l} + \sin\theta}{t\cos\theta\left[\frac{\cos^2\theta}{K_{hf}} + \frac{\frac{2h}{l} + \sin^2\theta}{K_s}\right]} \tag{4}$$

$$G_{xy} = \left[\frac{t\left(\frac{h}{l}\right)^2\left(1 + \frac{2h}{l}\right)\cos\theta}{K_{hf}\left(\frac{h}{l} + \sin\theta\right)} + \frac{t\left(1 + \frac{h}{l}\sin\theta\right)^2}{K_s\cos\theta\left(\frac{h}{l} + \sin\theta\right)}\right]^{-1} \tag{5}$$

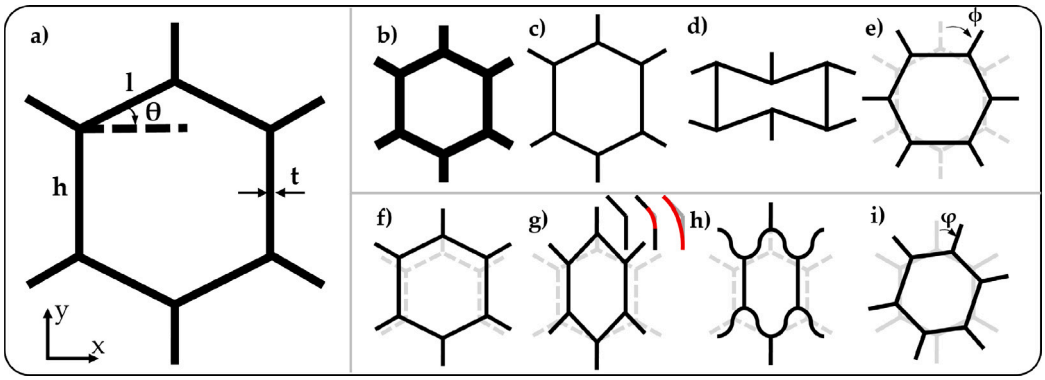

Fig. 2. Hexagonal honeycomb unit cell (a) dimensions (regular honeycomb), (b) to (e) examples of modified cell parameters; (b) increased wall thickness, (c) longer vertical wall, (d) decreased (negative) oblique wall angle, and (e) global rotation (of 30°), and (f) to (i) deformation types; (f) stretching walls, (g) hinging at wall junctions, with the relative length over which hinging would occur (q) covering none, half, and all of the joining walls, shown in red in the excerpt, (h) flexing walls, and (i) cell rotation. Lighter dashed lines show undeformed regular cell.

whereby E, ν, & G are Young's modulus, Poisson's ratio, and shear modulus (respectively). The two subscripts denote loading direction and plane (respectively). Force constants for flexing (K_f), hinging (K_h), and combined flexing and hinging (K_{hf}) are normalised to that of wall stretching (K_s):

$$K_s = \frac{E_s wt}{l} \tag{6}$$

$$K_f = \frac{E_s wt^3}{l^3} \tag{7}$$

$$K_h = \frac{E_s wt^3}{6l^2 q} \tag{8}$$

$$\frac{K_{hf}}{K_s} = \frac{t^3}{l^2 + 6lq} \tag{9}$$

whereby the subscript s denotes a property of the constituent material, and q is the length of the wall where hinging takes place [40]. Hinging can also happen via. shearing of wall junctions, but the developed force constant is generally high, so there is negligible deformation [40,39]. Previously, q has been approximated as around 0.1 to 0.2 [40,39]. Here, a curve was fit based on cell geometry, and parameters observed to either increase or decrease the relative hinge length:

$$q = \frac{q_{c0}}{t \times h_0^{q_{c1}} \times \cos^{q_{c2}}(\Phi^{q_{c3}})} \tag{10}$$

whereby $q_{c0} = 0.45$, $q_{c1} = q_{c2} = 2$, $q_{c3} = 3$, and Φ is the angle between the loading direction and a plane of symmetry (Supplementary Materials S4). The coefficient q was limited to between 0 and 1 [40].

The homogenised/global strain (ϵ) terms in the x and y-axis are:

$$\epsilon_x = \ln\left(\frac{X}{X_0}\right) = \ln\left(\frac{l\cos\theta - \delta\sin\theta}{l_0\ \cos\theta_0 - \delta_0\ \sin\theta_0}\right) \tag{11}$$

$$\epsilon_y = \ln\left(\frac{Y}{Y_0}\right) = \ln\left(\frac{h + l\sin\theta + \delta\cos\theta}{h_0 + l_0\ \sin\theta_0 - \delta_0\ \cos\theta_0}\right) \tag{12}$$

whereby X and Y are the unit cell side lengths, δ is wall deflection due to flexing, and the subscript 0 denotes a dimension before deformation.

The strain dependent off-axis loading of hexagonal honeycombs can be calculated using standard elasticity tensor transformation [40,39,53]. The expression for the Poisson's ratio, when loading is offset by an angle (ϕ) (Fig. 2e), is:

$$\nu_{yx}(\phi) = E_y(\phi)\left[\frac{(\cos^4\phi + \sin^4\phi)\nu_{yx}}{Ey} - \cos^2\phi\sin^2\phi\left(\frac{1}{E_x} + \frac{1}{E_y} - \frac{1}{G_{xy}}\right)\right] \tag{13}$$

where;

$$E_y(\phi) = \left[\frac{\cos^4\phi}{E_y} + \cos^2\phi\sin^2\phi\left(\frac{1}{G_{xy}} - \frac{2\nu_{yx}}{E_y}\right) + \frac{\sin^4}{E_x}\right]^{-1} \tag{14}$$

and;

$$\epsilon_y(\phi) = \epsilon_y\cos^2\phi + \epsilon_x\sin^2\phi \tag{15}$$

Equations for the orthogonal values $E_x(\phi), \nu_{yx}(\phi)$, and strain $\epsilon_x(\phi)$, are not required, as these can be obtained by adding 90° to the offset angle. Stress (σ) at strain increments during the region of deformation is:

$$\Delta\sigma_x = E_x\Delta\epsilon_x \tag{16}$$

$$\Delta\sigma_y = E_y\Delta\epsilon_y \tag{17}$$

which can be combined using tensor notation:

$$\nabla\cdot\sigma_{ij} = C_{ijkl}\nabla\cdot\epsilon_{ij} \tag{18}$$

whereby C is a rank-4 elasticity tensor. Integrating in the limit of infinitesimal strain:

$$\int_{\sigma_{ij(0)}}^{\sigma_{ij}} \nabla\cdot\sigma_{ij} = \int_{\epsilon_{kl(0)}}^{\epsilon_{kl}} C_{ijkl}\nabla\cdot\epsilon_{kl} \tag{19}$$

equation 18 becomes:

$$\sigma_{ij} = C_{ijkl}\,\epsilon_{kl} + \sigma_{ij}^0 \tag{20}$$

whereby the superscript 0 denotes the undeformed state. Eq. (20) can be summed over increments of strain (n):

$$\sigma_{ij}^{n+1} = C_{ijkl}^n\,(\epsilon_{kl}^{n+1} - \epsilon_{kl}^n) + \sigma_{ij}^n \tag{21}$$

providing a constitutive equation to calculate stress at various increments of strain.

2.1.2. Buckling

A column, wall, or slender cell, will buckle when subject to a (predictable) compressive load. The onset of buckling in a cell wall happens when axial compressive force reaches a critical value (F_c) [4,54,55]:

$$F_c = \frac{n_c^2\pi^2 E_s I}{L^2} \tag{22}$$

whereby I is the column's 2nd moment area ($wt^3/12$ for rectangular sections), and L is the column's length. The constant n_c relates to degrees of freedom of columns ends, and the shape which the buckled column takes [54]. Regular hexagonal honeycomb cells have three typical buckling modes, although only one usually occurs during uniaxial compression [17]. Buckling of two walls around each junction, and rotation/flexure of the third, causes adjacent rows of unit cells to rotate in opposite directions, breaking symmetry to become chiral [4,56–58,17], (Fig. 3a). The constant n_c is usually estimated after collecting

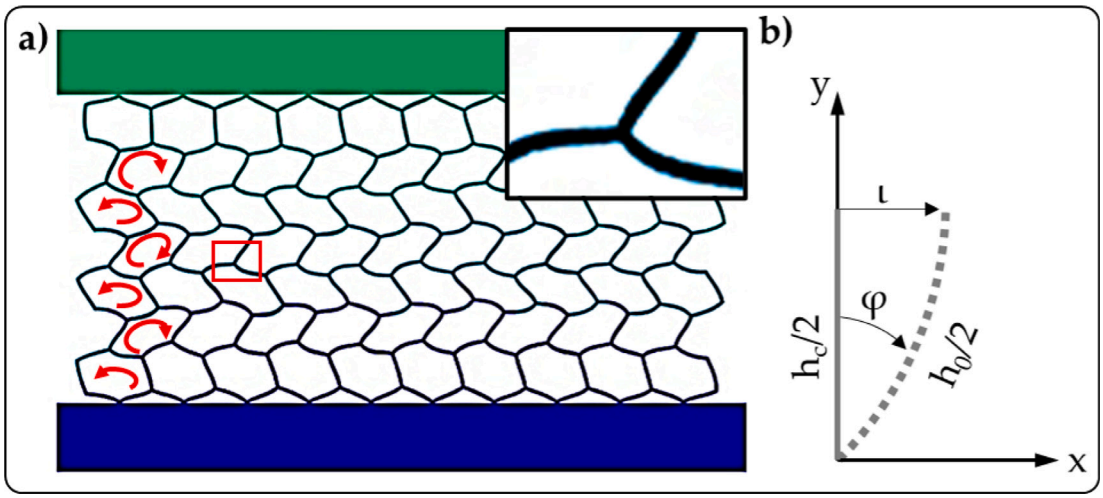

Fig. 3. (a) Asymmetric vertical wall buckling and cell rotation of a honeycomb in compression, (b) Half a buckling wall — where by the respective solid and dashed grey lines represent the compressed and buckled walls, and the origin marks the centre of the wall.

empirical data [4,56–58], so is unsuitable for a predictive model where cell parameters can change.

The closed form terms to predict the buckling of regular honeycombs are based on a non-dimensional value Q [17]:

$$Q_{ijk} = \sqrt{3\sqrt{3\sigma_{ijk}}} \tag{23}$$

where the indices i, j, or k denote normal stress parallel to the vertical wall (h), or either oblique wall (l_1 or l_2):

$$Q_i \tan\left(\frac{Q_i}{2}\right) - Q_j \cot\left(\frac{Q_j}{2}\right) - Q_k \cot\left(\frac{Q_k}{2}\right) \approx 0 \tag{24}$$

which can be rearranged to predict which of the three joining walls will cause buckling. As buckling can occur for Eq. (24) solutions close to zero [17], local minima of the square of the output of Eq. (24), that were also less than one, were selected to define the onset of buckling.

2.1.3. Post-buckling

Buckling causes wall flexure and hinging. Consider the vertical wall (h), following application of a load in the y-axis (Fig. 3b), and symmetric buckling (noting that h can be exchanged for l when the oblique walls buckle). The length at the point of buckling (h_c) may be lower than the curved wall length (h_0), which is the same as the wall's unloaded length (following the assumption that any normal load is removed at the point of buckling). The buckled wall is assumed to be symmetric. A function of the chord length (h_c), arc length (h_0) and angle of deflection (φ):

$$f\varphi = \sin(\varphi) - \frac{h_c}{h_0}\varphi = 0 \tag{25}$$

cannot be directly solved for φ, but can be approximated numerically using the Newton–Raphson method [59]:

$$\varphi_n = \varphi_{n-1} - \frac{f\varphi_{n-1}}{f'\varphi_{n-1}} \tag{26}$$

where:

$$f'\varphi = \cos(\varphi) - \frac{h_c}{h_0} \tag{27}$$

Here, an initial estimate for φ, of 10°, was used, and $n = 10$ iterations were specified for convergence, although convergence was generally reached when n reached 5 (with $|\varphi_{n+1} - \varphi_n|$ reaching $< 1E^{-8}$). Given that the radius of curvature (R) is $h_0/2\varphi$, the maximum deflection from the neutral axis (ι) is:

$$\iota = R\cos(1-\varphi) = \frac{h_0}{2\varphi}\cos(1-\varphi) \tag{28}$$

Knowing the flex in the vertical wall, and length of hinge at the wall junction, it is possible to introduce flexure constants (e.g., K_{hfb}), which take the form of the previous force constants (e.g., K_{hf}), and are calculated in the same way (Eqs. (6) to (9)), exchanging l for h as needed. The term q is set to the wall length (e.g., h_0), based on the assumption that the whole wall forms a hinge. While these relate to a pair of walls in each unit cell, buckling of one unit cell typically causes buckling of the other two walls at each junction [4,17]. These are also assumed to cause junctions to move towards each other, acting in the same direction as K_s. So, these force constants were divided by 3, and combined with K_s:

$$K_{shfb} = \left[\frac{1}{K_s} + \frac{1}{K_{hfb}}\right]^{-1} \tag{29}$$

The change in effective wall length (i.e., distance between junctions) following the application of a known stress can now be calculated. Two force constants contribute to the deflection:

$$K_{fb} = \Delta F / \Delta\delta_h \tag{30}$$

$$K_{hb} = \Delta M / \Delta\varphi \tag{31}$$

whereby:

$$\Delta F = \frac{\Delta\sigma_y X \sin\varphi}{2} \tag{32}$$

$$\Delta M = \frac{\Delta\sigma_y X \iota \sin\varphi}{2} \tag{33}$$

so, for each buckling, vertical wall:

$$\Delta\delta_{hb} = \frac{\Delta\sigma_y X \sin\varphi}{2K_{fb}} \tag{34}$$

$$\Delta\varphi = \frac{\Delta\sigma_y X \iota \sin\varphi}{2K_{hb}} \tag{35}$$

when normalised to depth. φ changes with wall rotation:

$$\Delta\varphi = \frac{\Delta\theta K_{hf}}{K_{hfb}} \tag{36}$$

For flexure in the limit of infinitesimal deformations:

$$\frac{d\delta_{hb}}{d\varphi} = \frac{K_{hb}}{\iota K_{hf}} d\varphi \tag{37}$$

so:

$$\int_{\delta_{hb(c)}}^{\delta_{hb}} d\delta_{hb} = \frac{K_{hb}}{\iota K_{hf}} \int_{\varphi_c}^{\varphi} d\varphi \tag{38}$$

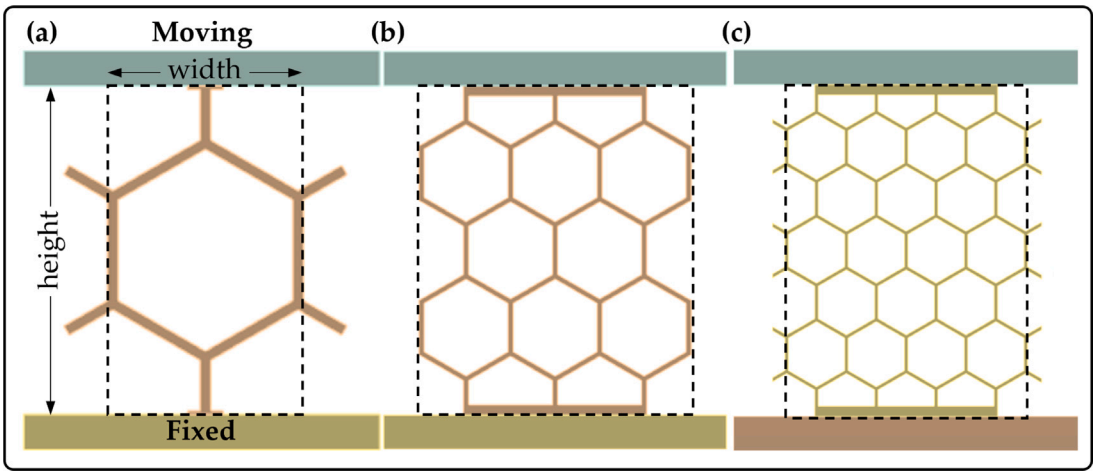

Fig. 4. Schematic showing dimensions and test/simulation set up for honeycombs with (a) one, (b) three and (c) 5 cells aligned vertically.

giving:

$$\delta_{hb} = \frac{K_{hb}}{K_{hf}} \frac{\varphi - \varphi_{(c)}}{\iota} + \delta_{hb(c)} \tag{39}$$

The distance between junctions that contributes to the global strains is updated ($h = h_o + \delta_h$), so the terms for strain (Eqs. (11) & (12)) remain unchanged. As the model predicts only buckled dimensions, there is a jump in strain after buckling. A linear interpolation of dimensions was used to allow better prediction of energy, and the onset of self contact/densification, through the buckling region.

For cases where the oblique walls buckle first, Eqs. (25) to (39) remain the same, although the buckling wall in the K_{hfb} calculation is exchanged form h to l (not included here for brevity). Incremental Poisson's ratios were obtained from the relative strains, while terms for the various moduli (Eqs. (1), (2) and (5)), and resulting stresses (Eq. (21)), were calculated as before (using the updated force constants and dimensions).

Considering asymmetric buckling, the unit-cell rotation develops over time. A-priori estimation of relationships between cell rotation and external loading are challenging [60,43]. Such micropolar materials (those showing internal rotations) are often characterised experimentally, or using microstructurally faithful numerical approaches [61,37,62]. In the assumption of infinite unit-cells, the macroscopic effect of micropolar tensors vanish, although the effect of unit cell orientation on macroscopic properties would not (e.g., Eqs. (13) to (15)). Here the effect of rotation on the homogenised response is considered (Eqs. (13) to (15)), rather than that of the strain energy stored by the rotation (i.e., micropolar effects [43]).

To obtain a relationship between unit cell rotation after the point of buckling ($\Delta\Phi$), and applied compression, recall Fig. 3b, related to buckling of the vertical wall:

$$\Delta\Phi = \tan^{-1}\left(\frac{2\iota}{h_y}\right) \tag{40}$$

where the subscript y denotes the vertical length of h_y. Should the oblique wall buckle:

$$\Delta\Phi = \tan^{-1}\left(\frac{2\iota}{l_{y\theta}}\right) \tag{41}$$

Noting:

$$\Phi = \Delta\Phi + \Phi_0 \tag{42}$$

After buckling, the newly developed deformation mechanism may cause the force that the structure can support to reduce. Such behaviour causes a response that is similar to negative stiffness [63]; with force reducing as deformation increases. To prevent divergence between experimental or FE data and the analytical model, an if statement was used, such that if the product of the post-buckling modulus and global strain were less than the current stress, the applied incremental modulus (Eq. (14)) was multiplied by −1.

2.1.4. Self contact

The onset of the final deformation region, self-contact/densification, is approximated based on the distance between the centre of opposing cell walls. With cell rotation, and non-uniform flexure along cell walls, it is possible that first contact may not happen at the centre of the cell walls. To accurately simulate such self-contact would likely require a numerical rather than analytical model. As self-contact should be avoided when designing protective equipment [4,64], a safety factor was defined in the function approximating its onset, to reduce the risk of the analytical model over-predicting the point of self-contact. To apply the safety factor, relative wall thickness was multiplied by four, rather than the value of two that would be expected, as the distance between the two walls is a function of both of their thickness. With this safety factor applied, self-contact between opposing cell walls in the cell's y-axis would require:

$$h + 2l\sin\theta - 2(|\delta_h + \delta_b|)\cos\Phi_0 \; - 4t|\sin\theta| \leq 0 \tag{43}$$

or, in the cell's x-axis:

$$l\cos\theta - |\delta_h|\sin\Phi_0 - 4t|\cos\theta| \leq 0 \tag{44}$$

If either of the above conditions were met, modulus was approximated as the product of relative density and the relative modulus of the base material (as suggested before [4]), while Poisson's ratio was that of the base material.

2.2. Validation and verification

2.2.1. Design and fabrication

Honeycomb geometries (Table 1) were designed in computer aided design software (Dassault Systèmes, SolidWorks 2020). Group 1 (1, 3 & 5 cell variations with the same relative dimensions, Table 1) were fabricated and tested. All geometries were analysed numerically and analytically. Honeycombs were made by fused deposition modelling (Ultimaker 3.0), from thermoplastic polyurethane (Fillamentum/addi(c)tive polymers, TPU 98a [65]). A 0.2 mm layer height, and 100% infill were used, with the print path aligned along the length honeycomb walls.

Table 1
Honeycomb parameters varied within each group (excluding repeats).

Group:	1	2	3	4	5	6
Cells	1,3,5	3	3	3	3	3
θ_0 (°)	30	−20,10,0,15,30,45	30	30	30	30
Φ_0 (°)	0	0	15,45,90	0	0	0
t	0.10	0.133	0.133	0.05,0.2	0.133,0.2	0.133
h_0	1	1	1	1	0.75,1.5	1
height (mm)	48	40,49,45,40,48,53	50,48,48	48	54,42	48.5,44
width (mm)	20,40,30	43,45,46,44.5,40,33	38,30,38	40	58,35	40

Group 1: number of cells, 2: θ, 3: Φ, 4: t, 5: h, and 6: length of walls above/below the top and bottom cells. All samples were 40 mm deep. The asterisks in group 5 denote.

2.2.2. Experimental validation

The mass of honeycomb samples was recorded (Sartorius, AC210S), and compared to estimated values from the geometries and filament density (1200 kg/m^3 [65]). Honeycomb samples were compression tested using a mechanical test device (Hounsfield HK10s, 1 kN load cell, sampling at 30 Hz, Fig. 4), up to an effective compressive engineering strain of 80%, at an effective strain rate of 0.01 s^{-1}. The same honeycombs were then impacted with a flat plate on a bespoke, guided mass drop rig [66,67], at 1, 3 and 5 J (m = 2.615 kg, v = 0.88, 1.52, and 1.96 m/s, respectively - Fig. 4). Tests were filmed with a high-speed camera (Phantom Miro, R111 & Nikon, AF Nikkor 14,585 mm lens, 1200 × 800p, 24 Hz for compression tests, 500 × 300p, 8000 Hz for impact tests). Force was measured by four load cells (208C05-Force Sensor, PCB Piezotronics, sampling at 50 kHz), placed between the 10 mm thick carbon-steel plate the samples were resting on, and a massive anvil. Force data was filtered using a two pole, low-pass butter-worth filter with a cut off frequency of 5000 Hz. Displacements (the double integral of acceleration data from the force plate) were checked by tracking a dot on the impactor within camera footage (Supplementary Materials S3).

2.2.3. Numerical verification

The simulations matched the quasistatic and impact tests (Fig. 4). Hexahedral solid elements were used, with minimum element size set to a third of wall thickness (see Supplementary Materials S2 for mesh convergence study). To reduce computational cost, the honeycomb geometries were sliced to a thickness of 1 mm (0.3 mm for 5-cell samples, where thinner walls required a finer mesh). Deformation parallel to the honeycomb extrusion direction was set to zero on the sliced honeycomb faces, to prevent the thin geometries buckling, creating a quasi-2D problem while allowing the LS-Dyna self-contact formulation. Steel plates were used to apply deformation (by fixing one and setting an initial velocity or displacement on the other). These plates were made rigid for the impact simulations.

For the quasi-static simulations (ANSYS Mechanical, via. Ansy Workbench 2023 R1), bonded contacts were set between the compression plates and the samples. Frictional contacts (μ = 0.7) were defined between pairs of faces expected to undergo self contact, with a damping stabilisation factor of 0.1. Measured properties (Table 2), which were similar to those in the material data sheet, were applied [65] (see Supplementary Materials S1).

For the impact simulations (LS-Dyna, via. Ansy Workbench 2023 R1), methods were adapted from previous work using similar materials, load cases, and structures [35]. Frictional contacts (with static & dynamic μ = 0.7) were defined both between the plates and the honeycombs, and for self-contact between honeycomb walls. For both the rigid body contacts (between plates and honeycomb), and the self contacts, the segment-based contact setting, soft = 2 was applied. A time-step safety factor of 0.9 was used, with a maximum number of cycles of 10^8, over the ≤60 ms simulations. The default hourglass control (Flanagan–Belytschko Stiffness Form with exact volume integration; LS-DYNA ID (5) of 0.10) was used, with the default settings of quadratic bulk (1.5) and linear bulk (0.06). A first order polynomial hyper-elastic material model with a five term Prony series was applied (Table 2). All LS-Dyna acceleration data was filtered in MATLAB to remove vibrations, using two to four pole, low-pass butter-worth filters with cut off frequencies of ~2000 Hz.

Table 2
Material properties and models — see Supplementary Materials S1 for characterisation.

Material model	Co-efficient value		
1st Order polynomial (MPa)	C_{00}	C_{10}	C_{01}
	0	−47.563	63.548
Prony Series	α_i(MPa)	β_i	
i=1	52.00	10.0	
i=2	31.97	1.05	
i=3	18.22	0.10	
i=4	15.35	0.02	
i=5	15.03	0.01	
Properties			
ρ (kg/m^3)	E (MPa)	ν (kg/m^3)	G (MPa)
1200	114.00	0.45	34.45

2.2.4. Optimisation

An optimisation was undertaken for a 10 J impact of a 48 mm tall, 40 × 40 mm cross-section sample, using the analytical model, based on the established cellular solid selection requirements, that impact energy should be absorbed close to the point of densification [4,56]. A 15% factor of safety was defined (i.e. the optimisation was undertaken for an 11.5 J impact), based on model limits of agreement (see Supplementary Materials S6). Cell wall angles (θ) between −20° and 45° with 5° increments were first trialed, with the objective of maximising the length of the relative stress plateau. The optimal angle was stored, and the relative length of the vertical cell (h_0) was varied by increments of 0.01 between 0.75 and 1.5, with the same objective. Finally, the relative wall thickness was varied in increments of 0.01, so that the model predicted that all 11.5 J would be absorbed at a deformation marginally below the point of self contact/densification. Impacts of the final honeycomb geometry, and of stiffer/softer variants, were simulated in LS-Dyna, with the same settings as before (adjusting cell sizes to fit the required geometry).

3. Results

3.1. Experimental validation

Honeycomb compression generally followed the three well-known stages: linear (wall stretching, flexing and hinging), buckling induced stress plateau, then self contact (Fig. 5), as expected [4]. Between buckling and self-contact, rows of cells rotated in opposite directions, as expected [17]. Buckling happened two rows at a time, usually starting in the centre of samples, where edge effects (i.e. fewer constraining cells) were present. Both FE outputs and video footage were visually similar, with deformation vectors and contour plot values also matching (Fig. 5).

Close fit (i.e. force within 5% at equivalent displacement increments) was seen between experiment and FE simulation, both during quasistatic tests (Fig. 6) and impact tests (Fig. 7). The analytical model

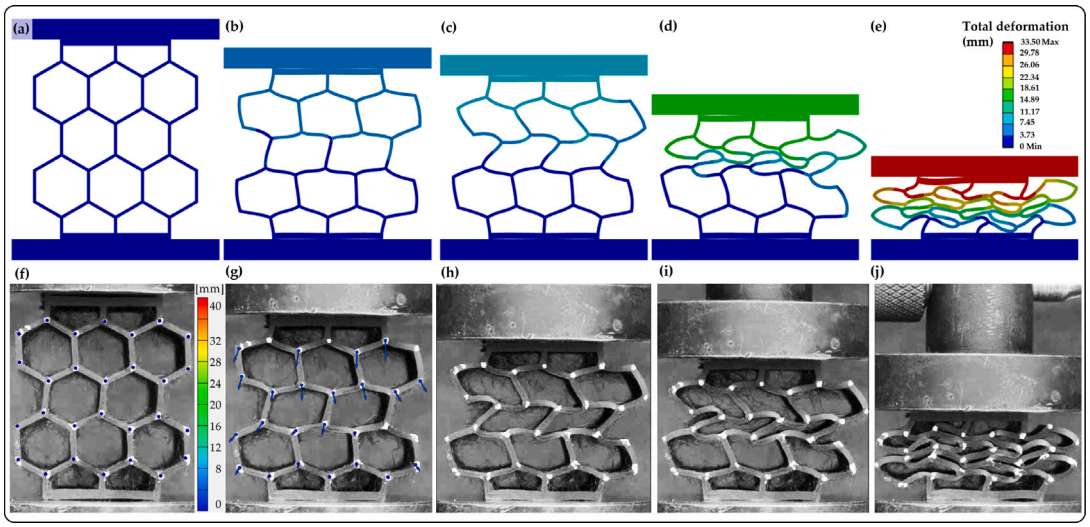

Fig. 5. (a) to (e) FE contour plots, and (f) to (j) test footage (with vectors from GOM Correlate in f) and (g)) showing total deformation during the static analysis of a 3-cell honeycomb (a) & (f) uncompressed, (b) & (g) before buckling, (c) & (h) immediately after buckling, (d) & (i) at the onset of self-contact, (e) & (j) at maximum compression.

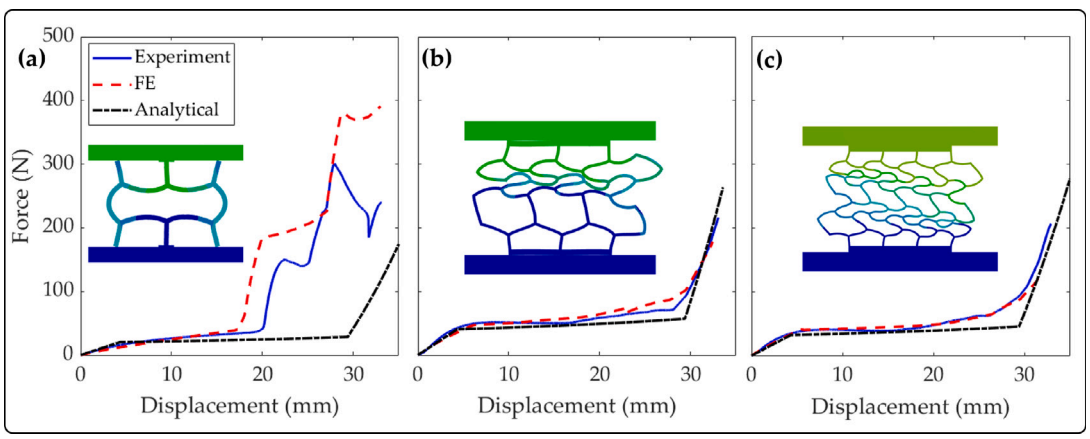

Fig. 6. Force vs. displacement for tests and numerical/analytical simulations of honeycombs in compression, with (a) one, (b) three and (c) five cells aligned vertically.

was then usually within ~15% of the FE and experimental data — see Supplementary Materials S6. Contact of unconnected walls in the single cell honeycomb increased error between FE and experiment (to within 10% - Figs. 6a, 7a, d, g). The analytical model did not reflect this non-homogenised response, and so exhibited large error when non-connected walls contacted plates (Figs. 6a, 7a, d, g). The five-cell honeycomb impact tests and simulations still featured these unconnected walls, although their effect was relatively small, and so large errors were not seen (Fig. 7c, f, i).

3.2. Numerical verification

Following validation of the FE modelling approach, further verification of the analytical model was undertaken, by comparison to the FE model, using 3-cell honeycombs (Fig. 8). Again, analytical model forces at equivalent displacements were generally within ~15% of the FE data, as were peak forces and displacements (see Supplementary Materials S6). In some simulations, response after self-contact differed; the assumption in the analytical model that the response tends towards that of a continuum solid did not hold throughout, (e.g., $\phi = 15°$ in Fig. 8d, & all samples in Fig. 8e). Indeed, contact between cut walls and structural collapse of the whole honeycomb after self contact were seen during FE simulations of these impacts (Fig. 8d, g, h, i).

3.3. Optimisation

The optimisation suggested a honeycomb geometry with $\theta = 45°$, $h_0 = 1.15$, and $t = 0.15$ would reduce peak impact force from the initial ~2000 N to ~500 N (see Supplementary Materials S5 for iterations). The FE verification approximately agreed with the analytical model (Fig. 9), and demonstrative cases used to show the effect of stiffening ($\theta = 45°$, $h_0 = 1.2$, and $t = 0.16$) or softening the honeycomb ($\theta = 30°$, $h_0 = 1$, and $t = 0.1$, as used in the validations (Figs. 6 & 7)).

4. Discussion

The analytical model can approximate the response of honeycombs under large strain compression and impact, predicting force and displacement within ~15% of experiments and FE simulations (Figs. 7, 8, & 9, Supplementary Materials S6). The limits of agreement for energy absorbed at various displacement increments were between +15 and −9% of the FE simulations, with the analytical model typically predicting 3% higher energy at each increment (Supplementary Materials S6). The difference between the two models was caused by fluctuations in force readings in the FE model and experiments, but not the analytical one. Assumptions that contributed to these differences included sequential buckling of rows of cells [29,4,17], use of a rate adjusted, but

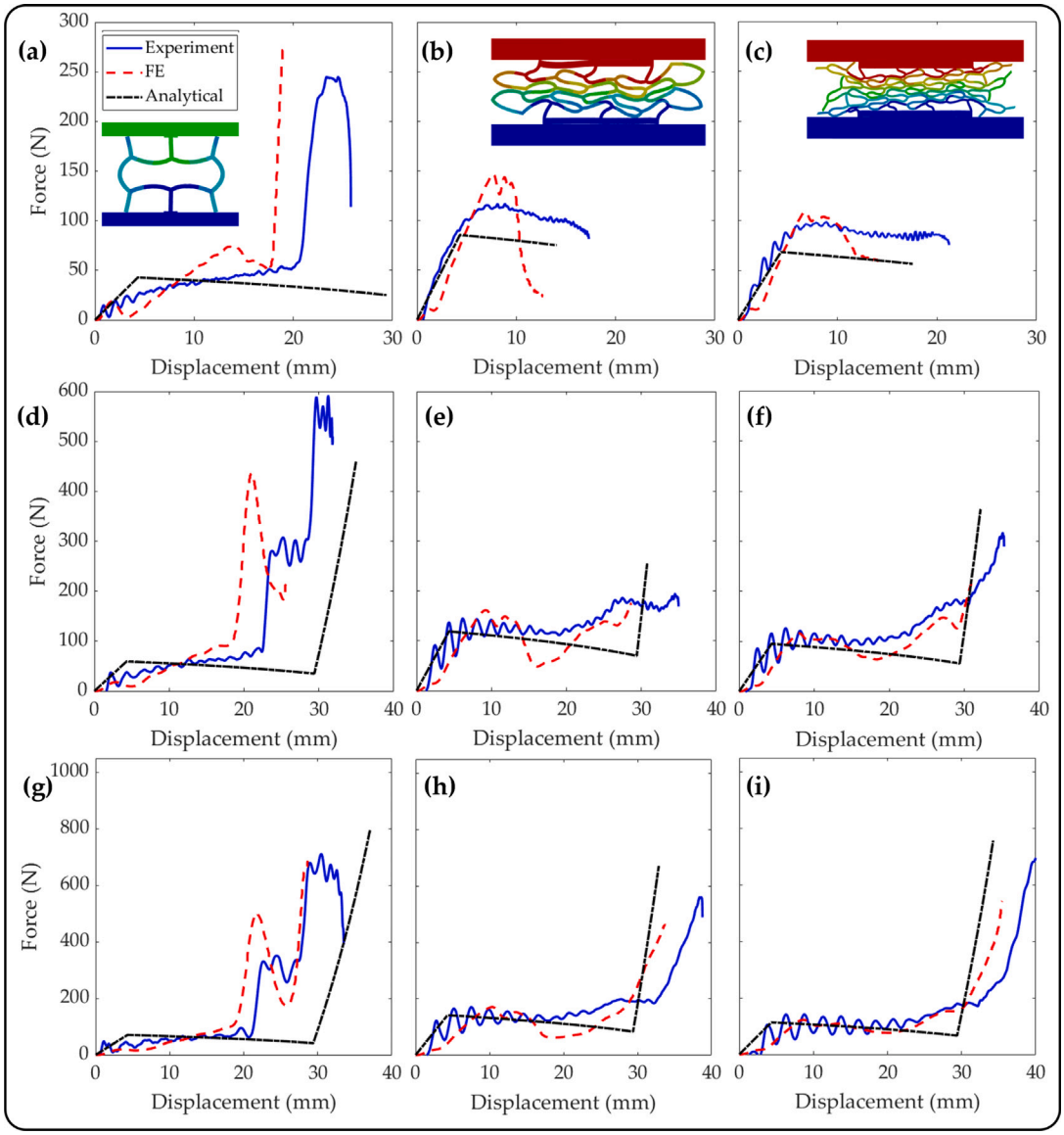

Fig. 7. Force vs. displacement for tests and numerical/analytical simulations of honeycombs during (a) to (c) 1 joule impacts, (d) to (f) 3 joule impacts, (g) to (i) 5 joule impacts, with (a), (d), & (g) one, (b), (e), & (h) three and (c), (f), & (i) five cells aligned vertically.

constant, modulus for the intrinsic material, and simplification of self-contact. Knowing it is limitations, the analytical model was used, with a safety factor of 15%, for a parametric optimisation (Fig. 9), reducing peak impact force by a factor of four, compared to a geometry used in the validations. The run time for the optimisation (with 32 trial geometries) on a laptop with 16 GB RAM was 0.6 seconds. Each FE simulation took between one and four hours on the same laptop. The reduction in optimisation time is indicative of reduced computational costs. The FE simulation time could be reduced by using more powerful CPU's, while the analytical model solver time would increase when using less powerful CPU's. As such, the model shows potential for efficiency savings within design cycles. It could be used to pre-select structures for FE or experimental optimisation, reducing the number of cycles required, or where time and data constraints prevent training of a machine learning model [46,20,38].

The analytical model used established functions to define the linear elastic region [4,40,39], and onset of buckling [17,51]. After buckling, new response functions were adapted from established ones [4,40,39], by modifying the relative length over which buckling occurs, and defining rotation of the unit-cells. Such responses are clearly seen in previous work, [4,17,51], although previous work has not reported analytical calculation of their effect (Eq. (23) to 42). The approximation of the onset of densification (Eqs. (43) and (44)) can be visually checked against force displacement plots, videos of compression and impact tests, and FE deformation maps (Figs. 5 to 9). The point of self contact was within 10% of the experimental/FE model value, and generally happened earlier in the analytical model, based on the applied safety factor.

The affect of passing, or not passing, the point of self contact/densification can be stark, while overly stiff samples also exhibit moderately higher peak forces (Fig. 9). These results highlight that certain parameters clearly affect proximity to the point of self contact. Changing wall thickness (Fig. 8a) affects stiffness — via. hinging, flexing and stretching constants, and the relative length over which hinging occurs (q), as expected [40,4]. Wall thickness also affects the onset of buckling, via. the wall second moment area [54], and the degree to which the end of each wall is constrained (n_c). Thicker walls also cause earlier onset of densification, as they will touch at lower levels of compression [4]. For these flat plate impacts, slender cells with low buckling strain and late densification were favourable (Fig. 9). Such

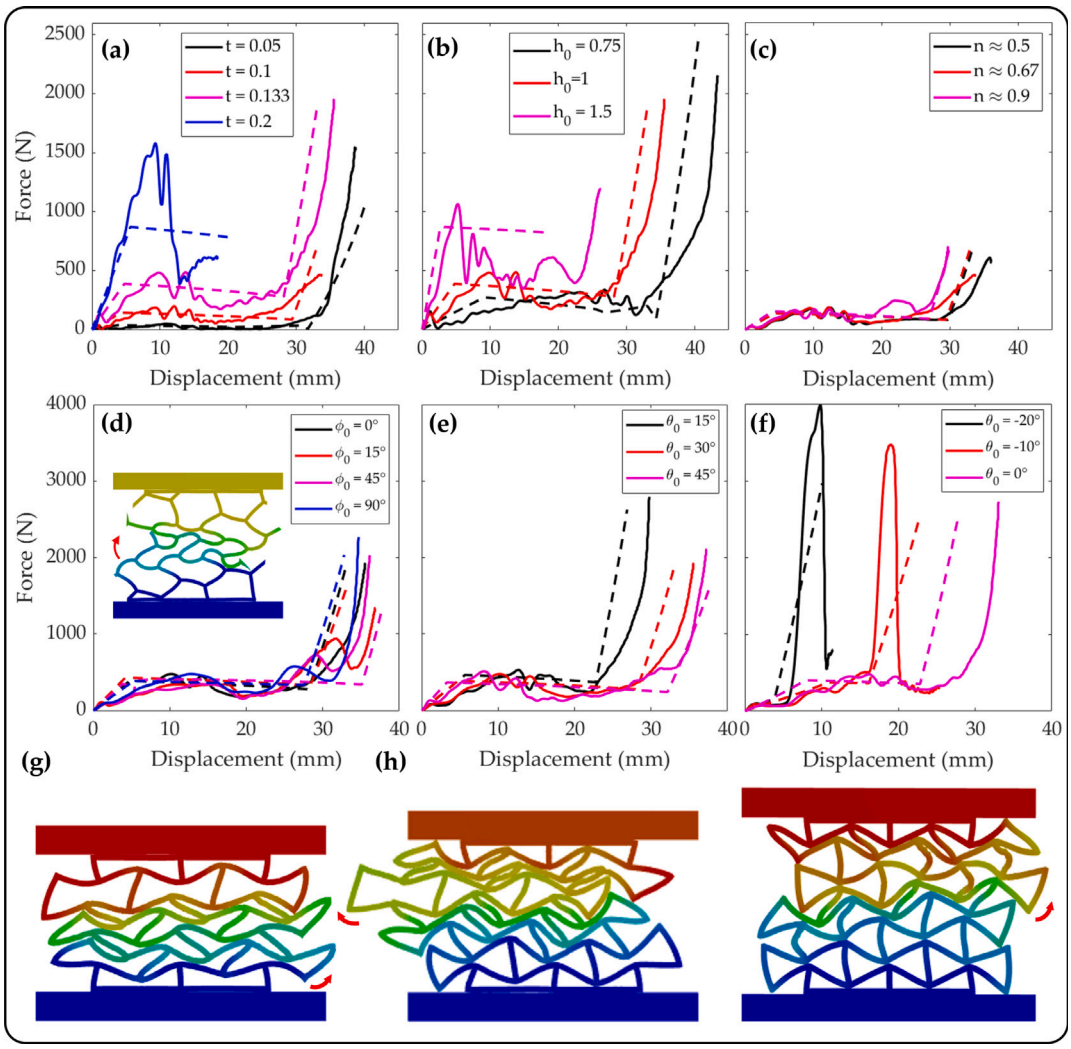

Fig. 8. (a) to (f) Force vs. displacement for FE and analytical simulations of honeycombs with varying cell parameters; (a) wall thickness, (b) length, (c) constraint type, (d) cell orientation, (e) & (f) wall orientation. All honeycombs with wall thickness above 0.1 were impacted at 15 J rather than 5 J, to show all deformation regions. (g) to (h) show FE contour plots of total deformation, of (g) $\theta = 0°$, (h) $\theta = -10°$, (i) $\theta = -20°$. Insert in (d) shows collapse of the $\phi = 15°$ sample (same legend as Fig. 5e).

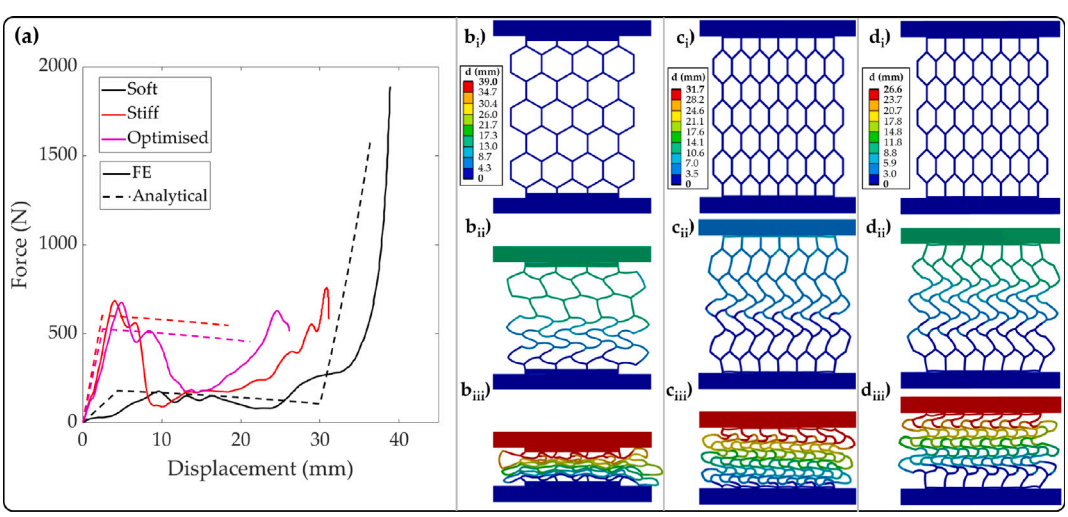

Fig. 9. (a) Force vs. displacement for FE and analytical simulations of the initial and optimised honeycombs during the 10 J impacts, (b) to (d) contour plots showing total deformation of the (b) initial (soft), (c) stiffened, and (d) optimised honeycombs (i) at the point of impact, (ii) immediately after wall buckling, & (iii) at maximum compression. Same legend for (b) to (d).

slender cells also have low transverse stiffness, which can be favourable in helmets where reducing shear stiffness can reduce harmful rotational accelerations [68]. Changing the oblique cell wall angle (θ) to negative values can cause negative Poisson's ratio (i.e. the honeycomb will contract laterally in compression [69,70]), sometimes beneficial during impacts with concentrated loads [1,71–74]. Here, changing the cell wall angle to negative values also caused early densification, and high peak forces (Fig. 8f). Where negative Poisson's ratio provides benefits, re-entrant cells could be coupled with long vertical cell walls, to mitigate early densification (Fig. 8b).

Certain assumptions within the analytical model caused errors, particularly when a low number of cells were considered (Fig. 7). The analytical model did not include unconnected cell walls, which may contact an impactor, or other cell walls. When single cells were used, wall junctions were free to rotate, meaning the analytical model over-predicted stiffness (Figs. 6 & 7). Sample edge effects also contributed to global buckling (Fig. 8). Indeed, care should be taken when notable divergence from assumptions of homogeneity (i.e. non-direct mapping between local and global stiffness tensors) are expected. The negative effective stiffness present after buckling was approximated in this model, as stress calculations (e.g., Eq. (21)) were cumulative. Further work could develop analytical models that directly calculate such force reductions.

A limitation of this model, that is also a known challenge for efficient simulation of such structures under large deformations [37,38], is the assumption of direct mapping between local and global stiffness. The analytical model does not simulate the observed locally ordered buckling, where rows collapsed sequentially (Fig. 5), as seen before [4,56,55]. Simulating different rows or cells as interconnected springs, or homogenised units with non-linear elasticity tensors [42,43,45,37,38], may allow better approximation of the map between local and global stiffness. The same approach could also facilitate fast design of locally tuned gradient [75] or hierarchical structures [16–20].

The analytical model contained an approximation of the relative length over which wall hinging occurred (q), as with other analytical honeycomb models (e.g., [4,56,17,49,50]). Indeed, this constant, the negative stiffness approximation, and the Newton–Raphson solution of bucking wall deflection, are not analytical, and should be interpreted with care when new constituent materials and sample dimensions are used. Further work could look to create more rigorous terms for q, perhaps by studying degrees of freedom around wall junctions in various sizes of sample, with varying constituent materials.

This study used hyper-elastic materials, low speed impacts, and compression tests, where substantial dynamic effects (i.e., variable/non-linear viscoelasticity [35], shock-waves, and micro-inertia), plasticity, or absolute failure, were not expected. While failure in thin walled structures often occurs at a similar compression level to elastic buckling [4,17,29], as this is the point at which deformation (particularly tensile and shear strain) increases rapidly, further work could specifically study and include these.

While the parametric optimisation presented here minimised peak force, other objectives such as the maximum rate of force application, or duration over a limiting threshold associated with injury or damage, would be possible [2,22,23]. The maximum rate of force increase was either in the linear elastic region, or after densification (if present), and was similar for the analytical model, and experimental/FE data (Figs. 6–9). The analytical model also contains unused information relating to wall flexing, local strain, and cell orientation. The cell rotations ranged from 0° to 45°, and were estimated to within 15° (see Supplementary Materials S6). These could be used to include plasticity or damage terms [44], or map micromorphic tensors to define the connection between local and global stiffness, when assumptions of homogeneity are not met [43].

Similarly, an expansion of the model to 3D lattices, or other cell types (e.g., chiral, or featuring different numbers of cell ribs/walls) would increase design degrees of freedom, with various options being proposed over the last few decades [76,17,4,35,13]. An interesting potential for further work could be to apply models such as these to obtain hyper-elastic material models, or those that also include terms for plasticity and damage. Only the 2D response was considered here, while approximating the out of plane response could also allow fast optimisation during concentrated, indenting loads, or with more loading orientations.

5. Conclusions

The developed analytical model approximated honeycomb large strain compression and low-speed impact response. The model agreed with numerical and experimental data, with force values usually within ~15% at each deformation increment, over a broad range of cell geometries. So, the model provides a fast approximation between cell geometry and response, that was used to suggest an optimal geometry for a given (10 J flat plate) impact, reducing peak force by a factor of four after a 0.6 second optimisation on a laptop with 16 GB RAM. The numerical simulations took one to four hours on the same laptop, indicative of reductions in computational cost. As such, this model could be used before FE or experimental development cycles, to improve mechanical metamaterial design efficiency, tune geometric parameters to suit different user requirements (such as body types or injury history), or adapt to environmental stimuli.

CRediT authorship contribution statement

Olly Duncan: Conceptualization, Data curation, Formal analysis, Investigation, Methodology, Project administration, Software, Validation, Writing – original draft, Writing – review & editing.

Declaration of competing interest

The authors declare that they have no known competing financial interests or personal relationships that could have appeared to influence the work reported in this paper.

Data availability

All data (geometries, experimental data, & Matlab scripts, and example FE simulation files (not all, as file size too large)) are stored on Mendeley-data (https://data.mendeley.com/datasets/5fwrmywjjs/1). Data can also be accessed via. the https://meta-genome.org, and the Matlab scripts also stored on Github [52]. Additional FE files can be provided by the author upon reasonable request.

Acknowledgements

The author would like to thank Gary Buller (Manchester Metropolitan University) for fabricating the test samples. No external funding was used for this project.

Appendix A. Supplementary data

Supplementary material related to this article can be found online at https://doi.org/10.1016/j.ijimpeng.2024.104973.

References

[1] Duncan O, Shepherd T, Moroney C, Foster L, Venkatraman P, Winwood K. Review of auxetic materials for sports applications: Expanding options in comfort and protection. Appl Sci 2018;8(6):941. http://dx.doi.org/10.3390/app8060941.

[2] Haid D, Foster L, Hart J, Greenwald R, Allen T, Pooya S, et al. Mechanical metamaterials for sports helmets: Structural mechanics, design optimisation, and performance. Smart Mater Struct 2023. http://dx.doi.org/10.1088/1361-665X/acfddf.

[3] Mills NJ. Polymer Foams Handbook: Engineering and biomechanics applications and design guide. Elsevier; 2007.

[4] Gibson LJ, Ashby MF. Cellular solids. Structure and properties. Cambridge: Press Syndicate of the University of Cambridge; 1997, http://dx.doi.org/10.1017/CBO9781139878326, 4, 67, 100, 103, 106, 109, 167–169, 176–183, 259–2.

[5] Leng B, Ruan D, Tse KM. Recent bicycle helmet designs and directions for future research: A comprehensive review from material and structural mechanics aspects. Int J Impact Eng 2022;168:104317. http://dx.doi.org/10.1016/j.ijimpeng.2022.104317.

[6] Singh O, Kumar Behera B. Review: A developmental perspective on protective helmets. J Mater Sci 2023. http://dx.doi.org/10.1007/s10853-023-08441-3.

[7] Horsfall I. Key issues in body armour: Threats, materials and design. Advances in military textiles and personal equipment. Woodhead Publishing Limited; 2012, p. 3–20. http://dx.doi.org/10.1533/9780857095572.1.3, URL http://dx.doi.org/10.1533/9780857095572.1.3.

[8] Mawkhlieng U, Majumdar A. Soft body armour. Text. Prog. 2019;51(2):139–224. http://dx.doi.org/10.1080/00405167.2019.1692583.

[9] Scher IS, Stepan L, Shealy JE, Hoover RW. Examining Ski Area padding for head and neck injury mitigation. J Sci Med Sport 2020. http://dx.doi.org/10.1016/j.jsams.2020.04.019.

[10] Sterzing T, Schweiger V, Ding R, Cheung JTM, Brauner T. Influence of rearfoot and forefoot midsole hardness on biomechanical and perception variables during heel-toe running. Footwear Sci. 2013;5(2):71–9. http://dx.doi.org/10.1080/19424280.2012.757810.

[11] Mohsenizadeh S, Alipour R, Shokri Rad M, Farokhi Nejad A, Ahmad Z. Crashworthiness assessment of auxetic foam-filled tube under quasi-static axial loading. Mater Des 2015;88:258–68. http://dx.doi.org/10.1016/j.matdes.2015.08.152.

[12] Zhu HX, Mills NJ. The in-plane non-linear compression of regular honeycombs. Int J Solids Struct 2000;37(13):1931–49. http://dx.doi.org/10.1016/S0020-7683(98)00324-2.

[13] Barchiesi E, Spagnuolo M, Placidi L. Mechanical metamaterials: A state of the art. Math Mech Solids 2019;24(1):212–34. http://dx.doi.org/10.1177/1081286517735695.

[14] Janbaz S, Narooe iK, Van MT, Zadpoor A. Strain rate-dependent mechanical metamaterials. Sci Adv 2020;6:616–33. http://dx.doi.org/10.1126/sciadv.aba0616.

[15] Nature mechanical metamaterials collection. 2022, URL https://www.nature.com/collections/iebdeffddc.

[16] Lakes R. Materials with structural hierarchy. Nature 1993;361:511-15(February):511–5, URL https://www.nature.com/articles/361511a0.pdf.

[17] Haghpanah B, Papadopoulos J, Mousanezhad D, Nayeb-Hashemi H, Vaziri A. Buckling of regular, chiral and hierarchical honeycombs under a general macroscopic stress state. Proc. R. Soc. Lond. Ser. A Math. Phys. Eng. Sci. 2014;470(2167). http://dx.doi.org/10.1098/rspa.2013.0856.

[18] Mousanezhad D, Haghpanah B, Ghosh R, Hamouda AM, Nayeb-Hashemi H, Vaziri A. Elastic properties of chiral, anti-chiral, and hierarchical honeycombs: A simple energy-based approach. Theor Appl Mech Lett 2016;6(2):81–96. http://dx.doi.org/10.1016/j.taml.2016.02.004.

[19] Mousanezhad D, Ebrahimi H, Haghpanah B, Ghosh R, Ajdari A, Hamouda AM, et al. Spiderweb honeycombs. Int J Solids Struct 2015;66:218–27. http://dx.doi.org/10.1016/j.ijsolstr.2015.03.036.

[20] Buehler MJ. Melm, a generative pretrained language modeling framework that solves forward and inverse mechanics problems. J Mech Phys Solids 2023;181(August):105454. http://dx.doi.org/10.1016/j.jmps.2023.105454, arXiv:2306.17525.

[21] Shi J, Li H, Xu F, Tao X. Materials in advanced design of personal protective equipment: A review. Mater Today Adv 2021;12. http://dx.doi.org/10.1016/j.mtadv.2021.100171.

[22] Payne T, Mitchell S, Halkon B, Bibb R. A systematic approach to the characterisation of human impact injury scenarios in sport. BMJ Open Sport Exerc Med 2016;2(1):e000017. http://dx.doi.org/10.1136/bmjsem-2015-000017.

[23] Hutchinson J, Kaiser MJ, Lankarani HM. The Head Injury Criterion (HIC) functional. Appl Math Comput 1998;96(1):1–16. http://dx.doi.org/10.1016/S0096-3003(97)10106-0.

[24] Ji S, Ghajari M, Mao H, Kraft, Reuben H, Hajiaghamemar M, Panzer MB, et al. Use of brain biomechanical models for monitoring impact exposure in contact sports. Ann Biomed Eng 2022;50:1389–408. http://dx.doi.org/10.1007/s10439-022-02999-w.

[25] Clayton EH, Genin GM, Bayly PV. Transmission, attenuation, and reflection of shear waves in the human brain. J R Soc Interface 2012;9(June):2899–910.

[26] Wei W, Evin M, Bailly N, Llari M, Laporte JD, Arnoux PJ. Spinal injury analysis for typical snowboarding backward falls. Scand J Med Sci Sports 2019;29(3):450–9. http://dx.doi.org/10.1111/sms.13342.

[27] Ekeland A, Rødven A, Heir S. Injury trends in recreational skiers and boarders in the 16-year period 1996–2012. In: Scher I, et al., editors. Snow sports trauma and safety. 2017, p. 3–16. http://dx.doi.org/10.1007/978-3-319-52755-0.

[28] Aare M, Kleiven S, Halldin P. Injury tolerances for oblique impact helmet testing. Int J Crashworthiness 2004;9(1):15–23. http://dx.doi.org/10.1533/ijcr.2004.0268.

[29] Thomas T, Tiwari G. Crushing behavior of honeycomb structure: A review. Int J Crashworthiness 2019;24(5):555–79. http://dx.doi.org/10.1080/13588265.2018.1480471.

[30] Qin L, Yang S, Li G, Wang G, Chen Z, Li H. Design and optimization of circular honeycomb lower limb protection device under blast impact. J. Sandw. Struct. Mater. 2023;1–22. http://dx.doi.org/10.1177/10996362231212555.

[31] Wang Z, Zhou Y, Wang X, Zhang X. Multi-objective optimization design of a multi-layer honeycomb sandwich structure under blast loading. Proc Inst Mech Eng D 2017;231(10):1449–58. http://dx.doi.org/10.1177/0954407016672606.

[32] Caserta GD, Iannucci L, Galvanetto U. Shock absorption performance of a motorbike helmet with honeycomb reinforced liner. Compos Struct 2011;93(11):2748–59. http://dx.doi.org/10.1016/j.compstruct.2011.05.029.

[33] Abayazid FF, Carpanen D, Ghajari M. New viscoelastic circular cell honeycombs for controlling shear and compressive responses in oblique impacts. Int J Mech Sci 2022;222(March):107262. http://dx.doi.org/10.1016/j.ijmecsci.2022.107262.

[34] Ramos H, Santiago R, Soe S, Theobald P, Alves M. Response of gyroid lattice structures to impact loads. Int J Impact Eng 2022;164(July 2021):104202. http://dx.doi.org/10.1016/j.ijimpeng.2022.104202.

[35] Shepherd T, Allen T, Winwood K, Venkatraman PD, Alderson A. Validation of a finite element modelling process for auxetic structures under impact. Phys Status Solidi b 2020;1900197.

[36] Novak N, Vesenjak M, Krstulović-Opara L, Ren Z. Mechanical characterisation of auxetic cellular structures built from inverted tetrapods. Compos Struct 2018;196:96–107. http://dx.doi.org/10.1016/j.compstruct.2018.05.024.

[37] Roudbari M, Jorshari T, Lü C, Ansari R, Kouzani A, Amabili M. A review of size-dependent continuum mechanics models for micro- and nano-structures. Thin-Walled Struct 2022;170(108562). http://dx.doi.org/10.1016/j.tws.2021.108562.

[38] van der Giessen E, Schultz PA, Bertin N, Bulatov VV, Cai W, Csányi G, et al. Roadmap on multiscale materials modeling. Model Simul Mater Sci Eng 2020;28(4). http://dx.doi.org/10.1088/1361-651X/ab7150.

[39] Duncan O, Allen T. Fabrication, characterisation and modelling of uniform and gradient auxetic foam sheets. Acta Mater 2017;126:426–37. http://dx.doi.org/10.1080/14786435.2019.1671998.

[40] Masters IG, Evans KE. Models for the elastic deformation of honeycombs. Compos Struct 1996;35(4):403–22. http://dx.doi.org/10.1016/S0263-8223(96)00054-2.

[41] Harkati A, Boutagouga D, Harkati E, Bezazi A, Scarpa F, Ouisse M. In-plane elastic constants of a new curved cell walls honeycomb concept. Thin-Walled Struct 2020;149(October 2019):106613. http://dx.doi.org/10.1016/j.tws.2020.106613.

[42] Wu L, Mustafa M, Segurado J, Noels L. Second-order computational homogenisation enhanced with non-uniform body forces for non-linear cellular materials and metamaterials. Comput Methods Appl Mech Engrg 2023;407:115931. http://dx.doi.org/10.1016/j.cma.2023.115931.

[43] Eringen A. Microcontinuum Field Theories. New York: Springer Science+Business Media; 1999, http://dx.doi.org/10.1007/978-1-4612-0555-5.

[44] Forest S. Micromorphic approach for gradient elasticity, viscoplasticity, and damage. J Eng Mech 2009;135(3):117–31. http://dx.doi.org/10.1061/(ASCE)0733-9399(2009)135:3(117).

[45] Eringen A, Şuhubi E. Nonlinear theory of simple micro-elastic solids–I. Int J Eng Sci 1964;2:189–203. http://dx.doi.org/10.1016/0020-7225(64)90004-7.

[46] Bastek J-H, Kochmann DM. Inverse-design of nonlinear mechanical metamaterials via video denoising diffusion models. Nat. Mach. Intell. 2023;5(December). http://dx.doi.org/10.1038/s42256-023-00762-x, arXiv:2305.19836.

[47] Ha CS, Yao D, Xu Z, Liu C, Liu H, Elkins D, et al. Rapid inverse design of metamaterials based on prescribed mechanical behavior through machine learning. Nature Commun 2023;14(1):1–11. http://dx.doi.org/10.1038/s41467-023-40854-1.

[48] Hohe J, Becker W. Effective stress-strain relations for two-dimensional cellular sandwich cores: Homogenization, material models, and properties. Appl Mech Rev 2002;55(1):61–87. http://dx.doi.org/10.1115/1.1425394.

[49] Adhikari S. The eigenbuckling analysis of hexagonal lattices: Closed-form solutions. Proc. R. Soc. Lond. Ser. A Math. Phys. Eng. Sci. 2021;477(2251). http://dx.doi.org/10.1098/rspa.2021.0244.

[50] Sorohan S, Constantinescu DM, Sandu M, Sandu AG. On the homogenization of hexagonal honeycombs under axial and shear loading. Part I: Analytical formulation for free skin effect. Mech Mater 2018;119:74–91. http://dx.doi.org/10.1016/j.mechmat.2017.09.003.

[51] Rayneau-Kirkhope DJ, Dias MA. Recipes for selecting failure modes in 2-d lattices. Extreme Mech Lett 2016;9:11–20. http://dx.doi.org/10.1016/j.eml.2016.04.004, URL http://dx.doi.org/10.1016/j.eml.2016.04.004.

[52] Duncan O. Honeycomb impact. 2023, URL https://github.com/OllyDuncan/HoneycombImpact.
[53] Hearmon RF. An Introduction to Applied Aniso-tropic Elasticity. London, UK: Oxford University Press; 1962, p. 12.
[54] Timoshenko SP, Goodier JN. Theory of elasticity, 3rd ed.. New York: McGraw-Hill, USA; 1970.
[55] Gibson LJ, Ashby MF, Zhang J, Triantafillou TC. Failure surfaces for cellular materials under multiaxial loads-I. Modelling. Int J Mech Sci 1989;31(9):635–63. http://dx.doi.org/10.1016/S0020-7403(89)80001-3.
[56] Gibson LJ, Ashby MF, Schajer GS, Robertson CI. The mechanics of two-dimensional cellular materials. Proc R Soc Lond Ser A Math Phys Eng Sci 1982;382:25–42..
[57] Papka SD, Kyriakides S. Biaxial crushing of honeycombs: - Part 1: Experiments. Int J Solids Struct 1999;36(29):4367–96. http://dx.doi.org/10.1016/S0020-7683(98)00224-8.
[58] Papka SD, Kyriakides S. In-plane biaxial crushing of honeycombs - : Part II: Analysis. Int J Solids Struct 1999;36(29):4397–423. http://dx.doi.org/10.1016/S0020-7683(98)00225-X.
[59] Garrett S. Introductory numerical methods. In: Introduction to Actuarial and Financial Mathematical Methods. 2015, p. 411–63. http://dx.doi.org/10.1016/b978-0-12-800156-1.00013-3.
[60] Gauthier RD, Jahsman WE. A quest for micropolar elastic constants. J Appl Mech Trans ASME 1975;42(2):369–74. http://dx.doi.org/10.1115/1.3423583.
[61] Frenzel T, Kadic M, Wegener M. Three-dimensional mechanical metamaterials with a twist. Science 2017;358(6366):1072–4. http://dx.doi.org/10.1126/science.aao4640.
[62] Lakes R. Experimental micro mechanics methods for conventional and negative Poisson's ratio cellular solids as cosserat continua. Trans. ASME, J. Eng. Mater. Technol. 1991;113(1):148–55. http://dx.doi.org/10.1115/1.2903371.
[63] Lakes RS, Lee T, Bersie A, Wang YC. Extreme damping in composite materials with negative-stiffness inclusions. Nature 2001;410(6828):565–7. http://dx.doi.org/10.1038/35069035.
[64] Mills NJ, Zhu HX. The high strain compression of closed-cell polymer foams. J Mech Phys Solids 1999;47(3):669–95. http://dx.doi.org/10.1016/S0022-5096(98)00007-6.
[65] Fillamentum. Flexfill TPU 98a natural. 2020, https://fillamentum.com/wp-content/uploads/2020/10/Technical-Data-Sheet_Flexfill-TPU-98A_26082019.pdf.
[66] Parisi M, Allen T, Cologna M, Pugno N, Duncan O. Indentation and impact response of conventional, auxetic, and shear thickening gel infused auxetic closed cell foam. Smart Mater Struct 2023;32:074004. http://dx.doi.org/10.1088/1361-665X/acd91c.
[67] Imam S, Driscoll H, Winwood K, Venkatraman P, Allen T. Efficacy of density in predicting the protective properties of padded clothing in rugby. In: Proceedings of the 13th conference of the International Sports Engineering Association, vol. 49, (38):2020, p. 1–7. http://dx.doi.org/10.3390/proceedings2020049038.
[68] Vanden Bosche K, Mosleh Y, Depreitere B, Vander Sloten J, Verpoest I, Ivens J. Anisotropic polyethersulfone foam for bicycle helmet liners to reduce rotational acceleration during oblique impact. Proc. Inst. Mech. Eng. H 2017;231(9):1–11. http://dx.doi.org/10.1177/0954411917711201.
[69] Lakes RS. Foam structures with a negative Poisson's ratio. Science 1987;235(4792):1038–40. http://dx.doi.org/10.1126/science.235.4792.1038.
[70] Wojciechowski KW. Remarks on Poisson ratio beyond the limits of the elasticity theory. J Phys Soc Japan 2003;72(7):1819–20. http://dx.doi.org/10.1143/JPSJ.72.1819.
[71] Evans KE, Alderson A. Auxetic materials: Functional materials and structures from lateral thinking!. Adv Mater 2000;12(9):617–28. http://dx.doi.org/10.1002/(SICI)1521-4095(200005)12:9<617::AID-ADMA617>3.0.CO;2-3.
[72] Duncan O, Allen T, Foster L, Alderson A. Effect of Poisson's ratio on the indentation of open cell foam. Eur J Mech A Solids 2023;99:104922. http://dx.doi.org/10.1016/j.euromechsol.2023.104922.
[73] Tahir D, Zhang M, Hu H. Auxetic materials for personal protection: A review. Phys. Status Solidi b 2022;259(12):1–13. http://dx.doi.org/10.1002/pssb.202200324.
[74] Attard D, Cauchi R, Gatt R, Grima JN. Smart cellular systems with pressure dependent Poisson's ratios. 2020;26(2):37–45. http://dx.doi.org/10.12921/cmst.2020.0000014.
[75] Kholoosi F, Galehdari SA. Design, optimisation and analysis of a helmet made with graded honeycomb structure under impact load. Int J Crashworthiness 2019;24(6):645–55. http://dx.doi.org/10.1080/13588265.2018.1506605.
[76] UK Parliament. Concussion in sport - inquiry. 2021, URL https://committees.parliament.uk/work/977/concussion-in-sport/.